Key parameters controlling the performance of catalytic motors

Maria J. Esplandiu,[1] Ali Afshar Farniya,[1] and David Reguera[2,a)]
[1]*Catalan Institute of Nanoscience and Nanotechnology (ICN2), CSIC and The Barcelona Institute of Science and Technology, Campus UAB, Bellaterra, 08193 Barcelona, Spain*
[2]*Departament de Física Fonamental, Universitat de Barcelona, C/Martí i Franquès 1, 08028 Barcelona, Spain*

The development of autonomous micro/nanomotors driven by self-generated chemical gradients is a topic of high interest given their potential impact in medicine and environmental remediation. Although impressive functionalities of these devices have been demonstrated, a detailed understanding of the propulsion mechanism is still lacking. In this work, we perform a comprehensive numerical analysis of the key parameters governing the actuation of bimetallic catalytic micropumps. We show that the fluid motion is driven by self-generated electro-osmosis where the electric field originates by a proton current rather than by a lateral charge asymmetry inside the double layer. Hence, the surface potential and the electric field are the key parameters for setting the pumping strength and directionality. The proton flux that generates the electric field stems from the proton gradient induced by the electrochemical reactions taken place at the pump. Surprisingly the electric field and consequently the fluid flow are mainly controlled by the ionic strength and not by the conductivity of the solution, as one could have expected. We have also analyzed the influence of the chemical fuel concentration, electrochemical reaction rates, and size of the metallic structures for an optimized pump performance. Our findings cast light on the complex chemomechanical actuation of catalytic motors and provide important clues for the search, design, and optimization of novel catalytic actuators. © *2016 AIP Publishing LLC.* [http://dx.doi.org/10.1063/1.4944319]

I. INTRODUCTION

The conversion of chemical energy into directed motion is a key point behind the high efficient performance of biomolecular machines. Inspired by nature, there is a growing interest in engineering novel artificial machines which can self-propel and carry out autonomous work "a la carte," mimicking the impressive molecular machinery in living organisms. Although challenging tasks lie ahead, many groups have started an intense activity in studying chemically powered motors and micropumps.[1–16] These systems nowadays have promising perspectives for *in vitro* applications in sensing,[17–19] manipulation of cargoes,[19–23] isolation of species,[24–26] or drug delivery,[27–31] to mention just a few examples. In the realm of self-propelled engines, bimetallic motors, which are powered by catalytic reactions at two different metals, stand out as reference candidates for understanding the chemical actuation mechanism.[1–6,32] In particular, catalytic micropumps, developed by the pioneering work of the groups of Sen, Mallouk, and co-workers[4–6] as the inverse and immobilized counterpart of bimetallic micro-swimmers, constitute the ideal platform to perform these studies. The way that catalytic reactions end up driving motion is a rather complex process since it involves the coupling of electrochemical reactions, electrostatics, mass and charge transport, and fluid flow. Although there is a big consensus that the main mechanism driving bimetallic motors is

reaction-induced electrokinetic phenomena, there are still many issues which remain unsettled.[3–6,32–34] The same happens with other chemically driven motors. For instance, it has been recently demonstrated that Janus swimmers made of Pt and an insulator are actuated by an electrokinetic process rather than by pure neutral self-diffusiophoresis as suggested by many previous studies.[35,36] Such paradoxical results evidence the need of more theoretical and experimental efforts to fully understand the chemomechanical actuation and to acquire higher levels of control on the motor propulsion.

Given the difficulties of an exact analytical approach,[5,37,38] scaling analysis and numerical simulations can become a powerful tool to shed light on the complex chemomechanical actuation of catalytic objects from a theoretical point of view.[32–34,38–42]

In this context, this work aims at performing a comprehensive and systematic numerical analysis of the influence of the different parameters involved in the actuation of bimetallic catalytic micropumps. This study provides a better understanding of the whole scenario behind this process which can be also extended to free-standing bimetallic swimmers. The output of this analysis helps to identify the main relevant variables affecting the motion and provides, at the same time, important clues on how to design more efficient catalytic actuators.

II. THEORY

As mentioned before, bimetallic micropumps[4–6,32] stand out as the most convenient setup to understand the basic

a)Author to whom correspondence should be addressed. Electronic mail: dreguera@ub.edu

mechanisms of catalytic propulsion since the motor immobilization facilitates a simpler experimental measurement and analysis.

The catalytic actuation is based on the oxidation and reduction of a fuel such as H_2O_2 on the constituent metals (anode and cathode) according to the electrochemical reactions schematized in Fig. 1(a). The oxidation of H_2O_2 and hence the proton generation take place at the anode, whereas the electrochemical reduction of H_2O_2 and consumption of protons happen at the cathode. The reaction generates a proton gradient and proton flux along the bimetallic structure which induces an electric field and fluid flow as shown schematically in Fig. 1(b).

At stationary conditions, such electrokinetic process is governed by the following set of coupled equations:

(a) The Poisson equation for electrostatics which relates the net local charge density ρ_e and the electrostatic potential φ,

$$-\varepsilon \nabla^2 \varphi = \rho_e, \tag{1}$$

where $\varepsilon = \varepsilon_r \varepsilon_0$ is the permittivity of the liquid and $\rho_e = \sum_i F z_i C_i$ is the charge density defined in terms of the Faraday constant, F, the molar concentration, C_i, and the valence, z_i, of each ionic species denoted by the subscript i.

(b) The stationary Stokes equations describing fluid motion at low Reynolds numbers,

$$\nabla \cdot \boldsymbol{v} = 0, \tag{2}$$
$$\eta \nabla^2 \boldsymbol{v} = \nabla p + \rho_e \nabla \varphi, \tag{3}$$

where $\boldsymbol{v}$ is the fluid velocity, p is the pressure, η is the fluid viscosity, and the fluid has been considered as incompressible.

(c) The Nernst-Planck equation for mass transport,

$$\boldsymbol{v} \cdot \nabla C_i = \nabla \cdot (D_i \nabla C_i + z_i F \mu_i \nabla \varphi C_i), \tag{4}$$

where D_i is the diffusion coefficient, μ_i is the mobility, and the subscript i denotes the different species. The mobility is connected to the diffusion coefficient through the Einstein relation as $D_i = \mu_i RT$, where R is the ideal gas constant and T is the absolute temperature.

(d) The electrochemical kinetics at the anode (j_O) and cathode (j_R) represented by the Frumkin-corrected Butler-Volmer equations,[34]

$$j_O = k_O C_R \exp\left(\frac{(1-\alpha)\, nF\Delta\psi_s}{RT}\right), \tag{5}$$

$$j_R = -k_R C_O \exp\left(\frac{(-\alpha)\, nF\Delta\psi_s}{RT}\right), \tag{6}$$

where k_O and k_R are the effective rate constants for the oxidation and reduction, respectively, C_R and C_O are the reduced and oxidized reactant concentrations, respectively, $\Delta\psi_s$ is the electrode potential drop at the Stern layer, α is a dimensionless number between 0 and 1 that describes the symmetry of the activation energy barrier for the reaction, and n is the number of exchanged electrons between the reduced (R) and oxidized (O) species. Only the forward reactions were considered for the electrochemical reaction kinetics. The potential drop at the Stern layer is defined as

$$\Delta\psi_S = \zeta_w - \psi_{electrode}, \tag{7}$$

where ζ_w is the zeta potential of the substrate and $\psi_{electrode}$ is the electric potential of the electrode. The potential drop across the compact Stern layer scales with ζ_w and with the ratio between the Stern layer length (λ_s) and the Debye length (λ_D or κ^{-1}) according to the equation[34]

$$\Delta\psi_S \propto \frac{\lambda_s}{\lambda_D}\zeta_w. \tag{8}$$

In the case of very low salt concentrations in the electrolyte, which are the standard conditions for the operation of bimetallic catalytic motors and pumps, the Debye length is on the order of hundreds of nanometers, whereas the thickness of the Stern-layer is typically a few molecules (i.e., about 1 nm). Thus, at low salt concentrations $\lambda_s/\lambda_D \ll 1$, and $\Delta\psi_S$ would be very small. As a consequence, following Eq. (7), the electrode potential becomes approximately equal to the zeta potential (i.e., $\psi_{electrode} \cong \zeta_w$), and the electrochemical currents (Eqs. (5) and (6)) for H_2O_2 decomposition (Fig. 1(a)) become simply proportional to the concentration of reactants[34]

$$j_O = k_O C_{H_2O_2}, \tag{9}$$

$$j_R = -k_R C_{H_2O_2} C_{H^+}^2. \tag{10}$$

Recently it has been shown that even at high concentration of salts, the exponential terms of Eqs. (5) and (6) exert
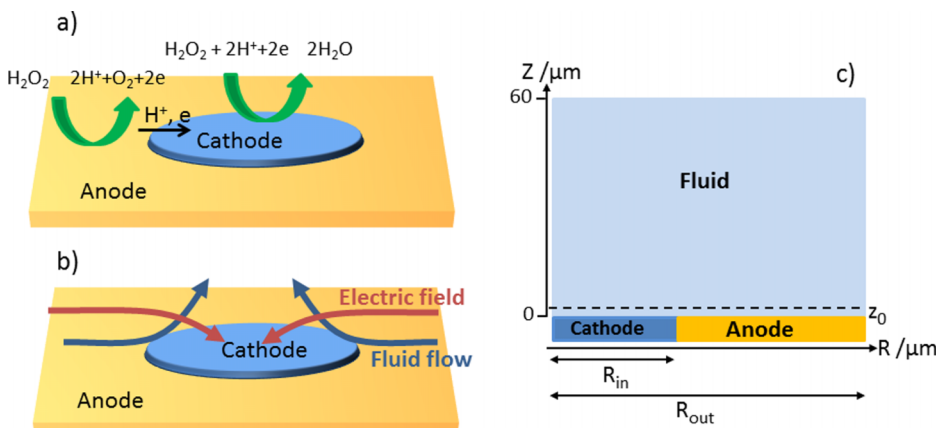

FIG. 1. (a) Typical setup of a bimetallic micropump, showing the electrochemical reactions taking place on it and leading to hydrogen peroxide decomposition. One metal acts as anode on which the peroxide is decomposed to produce protons and oxygen and the other metal acts as cathode consuming the generated protons. (b) Illustration of the resulting electric field (red arrows) and the fluid motion (blue arrows). (c) Scheme of the 2D axisymmetric system used for the simulations.

relatively little influence on the reaction kinetics in these catalytic systems.[40] Therefore, Eqs. (9) and (10) are good approximations for the electrode kinetics even at such conditions.

Finally, to avoid charge accumulation and to maintain steady-state conditions, we impose in the simulations, as in Refs. 34, 38, and 39, the current conservation constraint

$$J_{total} = \int_{anode} j_O dA + \int_{cathode} j_R dA = 0, \qquad (11)$$

i.e., the total amount of protons released into the solution at the anode per unit time equals the total amount of protons consumed at the cathode per unit time. This requirement is implemented in the simulations as a global constraint.

III. METHODS

In order to understand the main parameters controlling the performance of catalytic micropumps, finite element simulations using the software Comsol Multiphysics v4.3 were implemented. The studies were performed by solving the coupled governing equations, Eqs. (1)-(4) and (9)-(11). Figure 1(c) shows a scheme of the model system used for the simulations which corresponds to a bimetallic micropump with axial symmetry and variable radius for both metallic structures.

The simulation domain was discretized using an extremely fine mesh with 27 200 triangular elements that was refined using boundary layers near the electrode surface. A mesh density convergence study was performed to guarantee that discretization errors in the numerical solution are below 5% in all cases. Only stationary solutions were evaluated corresponding to steady state conditions. In the simulations, four different charged species have been considered: protons, hydroxide ions, and different stoichiometric salts. It is also assumed that the peroxide concentration is not significantly depleted by consumption (a hypothesis which is obviously not valid for very long times), and that a constant and uniform surface potential on the bimetallic structure ($\psi_{anode} = \psi_{cathode} = \psi_{substrate}$) is established. That is an approximation since the zeta potential can change

during the evolution of an electrochemical reaction at the surface.[43]

The following boundary conditions were defined for the electrode potential:

$$\varphi(z = z_{max}) = 0, \qquad (12)$$

$$\varphi(z = 0) = \psi_{substrate} = \zeta_w, \qquad (13)$$

where z_{max} corresponds to the upper boundary of the simulation system, typically placed at 60 μm above the surface (Fig. 1(c)). For the fluid velocity, stick boundary conditions were imposed on the substrate and slip elsewhere. For the concentrations of the different species, the bulk values were imposed at the upper boundary z_{max}. In the analysis, the values of the electric field, the fluid velocity, and the proton concentration were monitored at a distance $z_0 = 2$ μm above the surface. That is the typical distance at which those parameters have been estimated experimentally with colloidal tracers.[32]

The typical reference parameters used in the simulations are listed in Table I and will be kept fixed unless otherwise mentioned. These values mimic the standard experimental conditions for Pt-Au micropumps, as described in Ref. 32.

IV. RESULTS AND DISCUSSION

Figure 2 shows the spatial variation of the main electrokinetic parameters (fluid flow, electric field, local current of protons, charge density, and pH) obtained in a typical simulation using the parameters of Table I. The fluid flows from the anode to the cathode with a radial velocity which is especially large near the disk edge (see Fig. 2(a)). The fluid is then pumped upwards near the disk center to fulfill continuity. Figure 2(b) depicts the electric field, the current of protons, and the charge density in the fluid. As expected, the fluid is electroneutral above the double layer which has a thickness of about 200 nm at these conditions as shown in the zoomed image of Figure 2(c). The charge distribution inside the double layer is positive and asymmetric along the radial distance, with more positive charge accumulated on the anode as compared to the cathode. Interestingly, the electric field extends above the double layer in the region

TABLE I. Typical values of the parameters used in the simulations.

| Parameter	Description	Value
D_{H^+}	Proton diffusion coefficient	9.3×10^{-9} m^{2}s^{-1}
D_{OH^-}	Hydroxide ions diffusion coefficient	5.3×10^{-9} m^{2}s^{-1}
pH	Proton concentration in the bulk	5.6×10^{-4} mol m^{-3} ($pH = 6.25$)
$\zeta_{Cathode}$	Zeta potential of the cathode	-0.033 V
ζ_{Anode}	Zeta potential of the anode	-0.033 V
k_R	Rate constant of the cathode	0.1 m^{7}s^{-1}mol^{-2}
k_O	Rate constant of the anode	8.0×10^{-10} ms^{-1}
$[H_2O_2]$	H$_2$O$_2$ concentration	0.3M/300 mol m^{-3}/1% wt.
R_{in}	Radius of the cathode disk	15 μm
R_{out}	Radius of the anode ring	50 μm
$[A^+]$ and $[B^-]$	Concentration of additional monovalent ions in the solution	5 μm
D_A and D_B	Diffusion coefficient of the additional ionic species	1.0×10^{-9} m^{2}s^{-1}
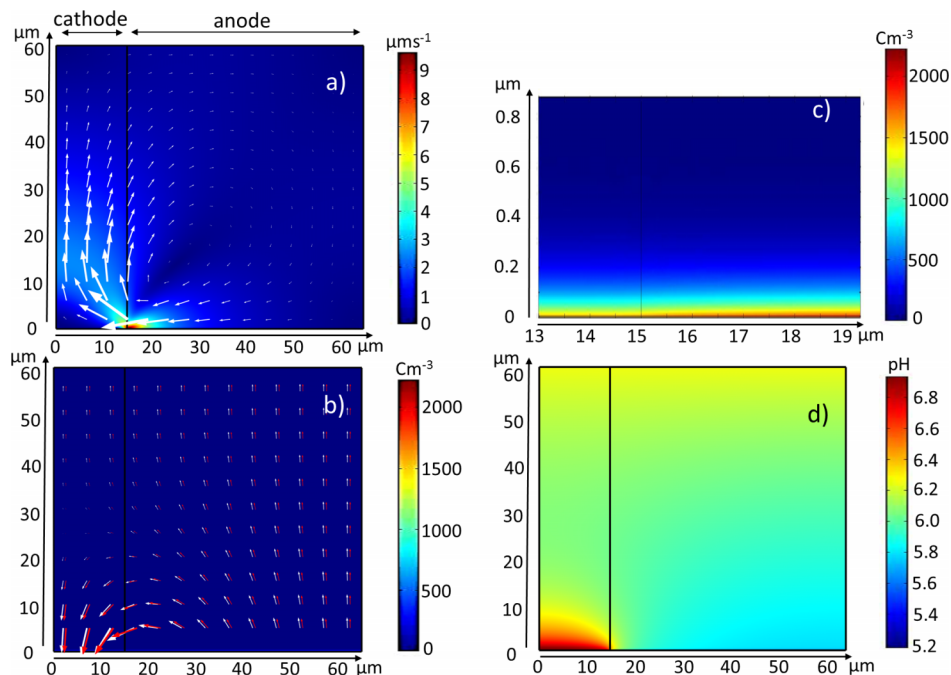
FIG. 2. Simulation results obtained using the parameters listed in Table I. (a) 2D fluid velocity field, where the arrows indicate the direction of the flow and the color scale the velocity modulus. (b) 2D electric field (red arrows), proton flow (white arrows), and charge density (indicated by the color scale). (c) Zoom of the charge density close to the surface, showing the electric double layer. (d) Spatial distribution of protons indicated by the local value of the pH.

of electroneutrality, as was also previously found in the simulation of bimetallic rods performed in Refs. 33 and 34. The electric field points from the anode towards the cathode and it is particularly intense near the disk edge. Its direction coincides with the local proton flux, evidencing that the electric field above the double layer is generated by the current of protons. This proton flow is fed by the electrochemical reaction that produces and consumes protons at the anode and cathode, respectively, generating a spatial gradient of pH illustrated in Fig. 2(d).

These results unveil clearly what is the relevant mechanism for the fluid pumping. The chemical reaction builds up a gradient of protons between the anode and the cathode. This gradient establishes a diffusion current that generates an electric field outside the double layer, following the Nernst-Planck equation, which in turn drives the fluid motion.

It is important to emphasize that the electric field driving all the electrokinetic phenomena occurring in the system is generated by the current of protons due to the chemical reaction and not merely by the asymmetry of charge inside the double layer. A net charge imbalance, and with it an electric dipole, is certainly present inside the double layer. However, this electric dipole is not the reason why an electric field is present outside the double layer driving the fluid motion. Instead, we want to clarify that the electric field is mostly generated by the diffusion current of protons induced by the proton gradient sustained by the chemical reaction. In fact, to verify this conclusion, we redid the simulation with no reactions but imposing a different charge density (or equivalently, surface potential) in the anode and cathode. At these conditions, the results show no significant electric field outside the double layer and no fluid motion, as one would expect, since the pumping is intrinsically a non-equilibrium process requiring a continuous supply of energy to sustain the flow.

To gain more insights of the chemo-mechanical mechanism, the impact of different variables on the most relevant parameters such as the electric field, fluid velocity, and local proton distribution are evaluated. Specifically the effect of the surface potential, salt concentration, rate constants, H_2O_2 and bulk proton concentrations, and size of the anode/cathode structures are analyzed in separate subsections.

A. Effect of the surface zeta potential

The surface potential is a key parameter for setting the electric double layer and triggering electrokinetic processes. As mentioned earlier, at low salt concentrations, the surface potential can be approximated by the zeta potential ζ_w. In general, zeta potentials of metals, such as Au and Pt, are negative, with typical gold values around -30 mV.[32] It is thus interesting to evaluate the effect of the value of the zeta potential on the double layer and on the catalytic actuation. Different values of the zeta potential could be reached either by using different metal electrodes, by chemical functionalization of the surface, or by polarization.

First, the charge density in the electric double layer at the anode and cathode was evaluated in presence of the electrochemical reaction for different values of the zeta potential. A similar study was performed in the case of bimetallic rods in Refs. 33 and 34 by changing peroxide concentration. As expected, negative surface potentials induce a net accumulation of positive charge, whereas positive surface voltages concentrate negative charge at the double layer on both cathode and anode (Figure 3(a)). However the charge density profiles inside the double layer (below 200 nm) become different at both electrodes when the catalytic reaction takes place (see Fig. 3(b)). The charge density at the anode is more positive than the one at the cathode generating a charge asymmetry inside the double
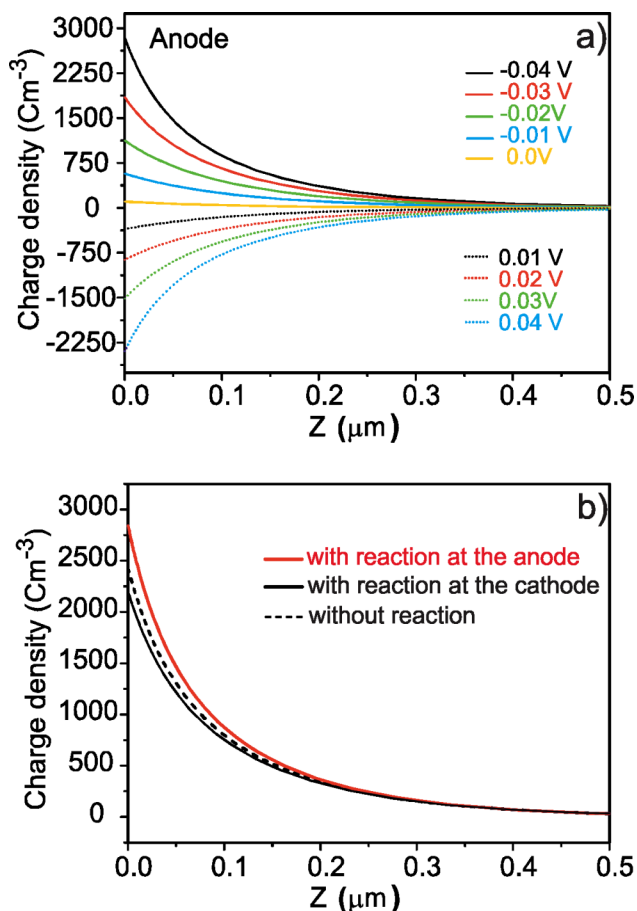
FIG. 3. (a) Charge density profile at the anode as a function of the distance from the surface for different values of the surface potential. (b) Charge density profile on the anode and cathode in the presence (solid lines) and absence (dashed lines) of the reaction. The surface potential is −0.04 V in this case.
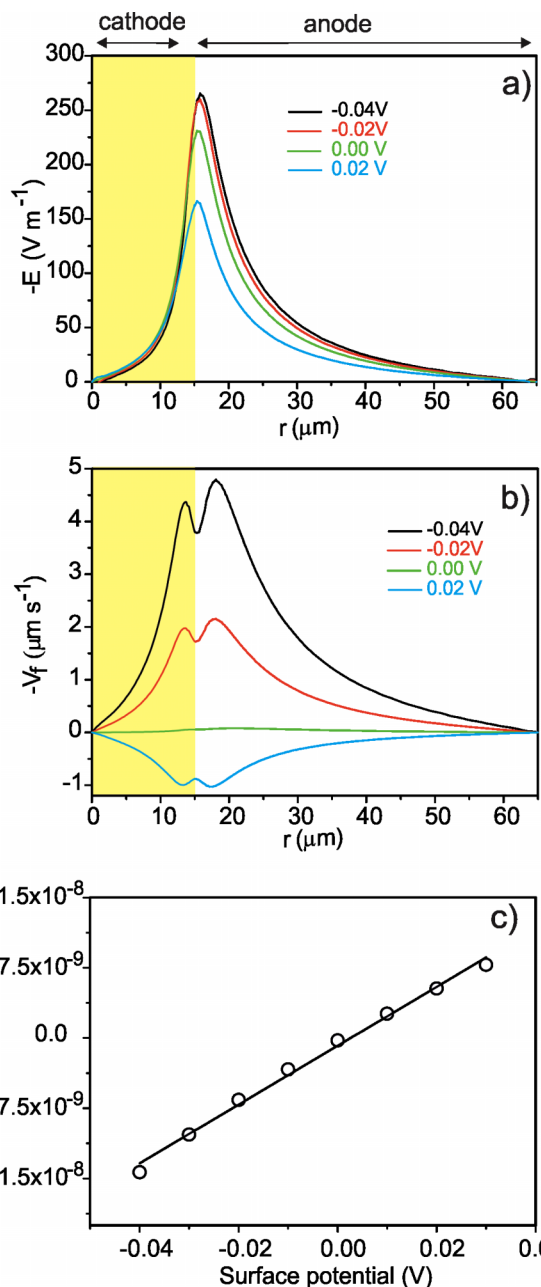

FIG. 4. Effect of the surface potential on the radial component of the electric field (a) and fluid velocity (b). The yellow area represents the area of the cathode. (c) Ratio of the maximum values of the radial velocity and the radial electric field, V_f/E, as a function of the surface potential, showing a linear behavior characteristic of electro-osmosis.

layer as previously discussed in Figure 2(c) and in Refs. 33 and 34.

Figures 4(a) and 4(b) shows the radial component of the electric field and fluid flow at a height of 2 μm above the double layer when the surface potential is varied from negative to positive values. (The effect of surface potential on the local proton concentration is analyzed on the supplementary material, Fig. S1.[44]) The electric field is attenuated as the surface potential becomes more positive, but does not change its directionality. Interestingly, the fluid velocity vanishes when the surface potential is zero (in agreement with the predictions of Posner and co-workers[34] for bimetallic rods) and inverts its direction when the substrate potential becomes positive. The inversion of the fluid flow can be rooted in the accumulation of negative charge inside the double layer at both electrodes when the surface potential is positive. The electric field which keeps pointing from the anode to the cathode will induce the motion of the negative charges towards the positive pole (anode) dragging the fluid in that direction.

These findings suggest that the pumping of the fluid occurs in a similar way as in an electro-osmotic process, where the electroosmotic fluid velocity V_{eo} is proportional to the electric field E and the zeta potential ζ_w, according to

$$V_{eo} = -\varepsilon \zeta_w \frac{E}{\eta}. \qquad (14)$$

In order to verify if that is the case, Fig. 4(c) plots the values of the maximum radial velocity V_f (measured at the disk edge, 2 μm above the surface) normalized with respect to the local value of the radial electric field E as a function of the zeta potential ζ_w. Indeed, Figure 4(c) shows a linear behavior with a slope of about 3×10^{-8} m^2/V s, similar to the expected value $\varepsilon/\eta = 7 \times 10^{-8}$ m^2/V s. This result confirms that the mechanism driving the fluid flow in these catalytic micropumps is indeed self-electroosmosis, i.e., electro-osmosis driven by an electric field which is

self-generated by the chemical reaction rather than being imposed externally. Therefore, the fluid velocity is mainly dictated by the zeta potential ζ_w and the electric field. So from now on, we will focus on the impact of the different relevant variables on the self-generated electric field, since the resulting fluid velocity will be directly proportional to it. Therefore, the variations in the electric field induced by the different parameters will have a direct translation in the fluid velocity.

B. Effect of the presence of an additional salt or other ionic species

Given the importance of the electric field to generate fluid motion, it becomes crucial to understand the effect of salts on the catalytic actuation. This topic is also relevant since it is impossible to experimentally address the catalytic motion in fluids completely free of ionic species. Figure 5(a) shows how the radial electric field at a distance of 2 μm from the electrode surface changes dramatically for different concentrations of a monovalent salt. As mentioned earlier, the same effect is observed in the fluid velocity, which is directly proportional to the electric field (see Figs. S2(a) and S2(b)[44]). The electric field and the velocity also decrease with the increase of salt valence (supplementary material, Figs. S3(a)
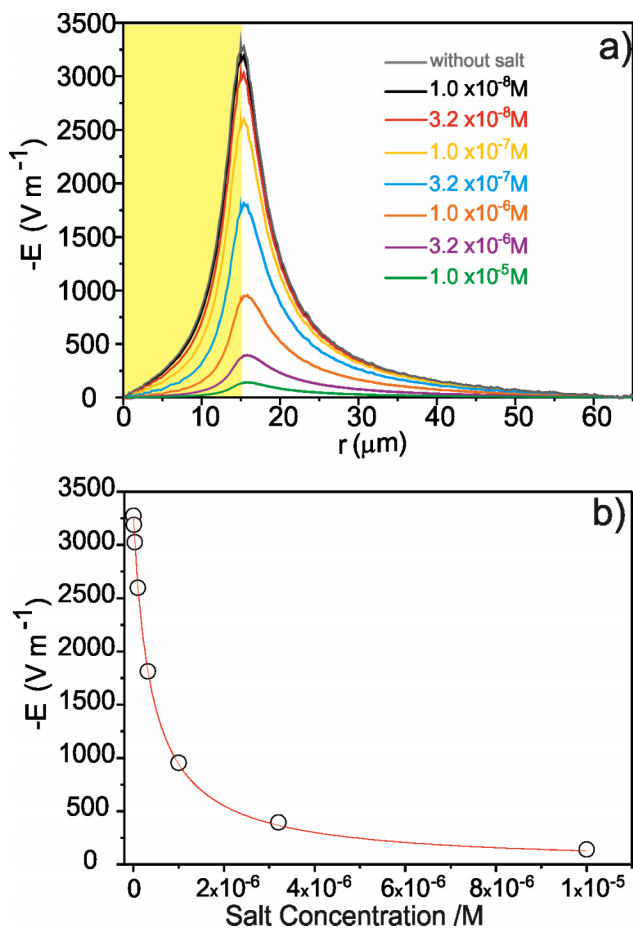

FIG. 5. (a) Dependence of the radial electric field with the concentration of a monovalent salt. (b) Decay of the maximum value of the radial electric field with the salt concentration. The red line represents the data fitted according to Eq. (15).

and S3(b)[44]). However, the addition of salt does not exert a very important impact either on the proton current or on the proton distribution at the anode and cathode (see Fig. S2(c) in the supplementary material[44]).

The electric field decay with increasing salt concentration is expected due to screening effects. As explained earlier, the electric field outside the double layer is generated by the current of protons. Hence, one would expect that its value should be sensitive to the conductivity of the medium according to Ohm's law,

$$E = \frac{j}{\sigma_{tot}} = \frac{j}{\sigma_o + bC_{AB}}, \qquad (15)$$

where j is the total current density due to all charged species, σ_{tot} is the total conductivity of the solution, being σ_o the conductivity given by H^+ and OH^- species, and bC_{AB} the conductivity associated with the introduction of the additional salt.

We have fitted the simulation data to Eq. (15), using the values of maximum radial component of the electric field and of the radial component of the current density at 2 μm above the surface determined from the numerical simulations. From the fit represented in Fig. 5(b) we have found $\sigma_0^{fit} = 3.07 \times 10^{-4} \pm 2 \times 10^{-6}$ S m^{-1} and $b^{fit} = 0.76 \pm 0.02$ S m^2/mol. In principle, for an ideal solution, one would expect theoretically that the conductivity and the molar ionic contribution of the additional salt are given by

$$\sigma_0^{th} = \frac{e^2}{k_B T} N_A (z_{H^+}^2 D_{H^+} C_{H^+} + z_{OH^-}^2 D_{OH^-} C_{OH^-}), \qquad (16)$$

$$b^{th} = \frac{2e^2}{k_B T} N_A (z_{A^+}^2 D_{A^+}), \qquad (17)$$

where k_B is the Boltzmann constant, N_A is Avogadro's number, z, D, and C are the charge, diffusion coefficients and concentrations of the different species, and the diffusion coefficient of the two ions has been considered to be the same ($D_{A^+} = D_{B^-}$). For the conditions used in the simulations, and listed in Table I, we have $\sigma_0^{th} = 2.73 \times 10^{-4}$ S m^{-1} and $b^{th} = 0.07$ S m^2/mol. Thus a reasonably good agreement is found for σ_o but not for b, where the theoretical estimate and the fit differ by one order of magnitude. This finding suggests that the electric field dependence with the salt concentration is not completely controlled by the fluid conductivity. To have a better understanding of these results, we repeated the simulations for different valences (up to 4:4) and concentrations of the additional salt, and plotted the results in Fig. 6(a) as a function of the total ionic strength of the solution. As can be seen, all the data collapse in the same curve. That indicates that the electric field decay (and accordingly the velocity, as shown in Fig. S3(c)[44]) is controlled by the ionic strength rather than by the total conductivity. Similar conclusions were found by Moran and Posner.[40] In order to confirm this observation, we repeated the simulations using different values of the diffusion coefficient of the additional salt. The results plotted in Fig. 6(b) show that neither the electric field nor the proton distribution (see supplementary material, Fig. S3(d)[44]) depend on the ion diffusion coefficients.

A simple argument can be made to justify why the electric field driving the fluid pumping depends on the ionic strength
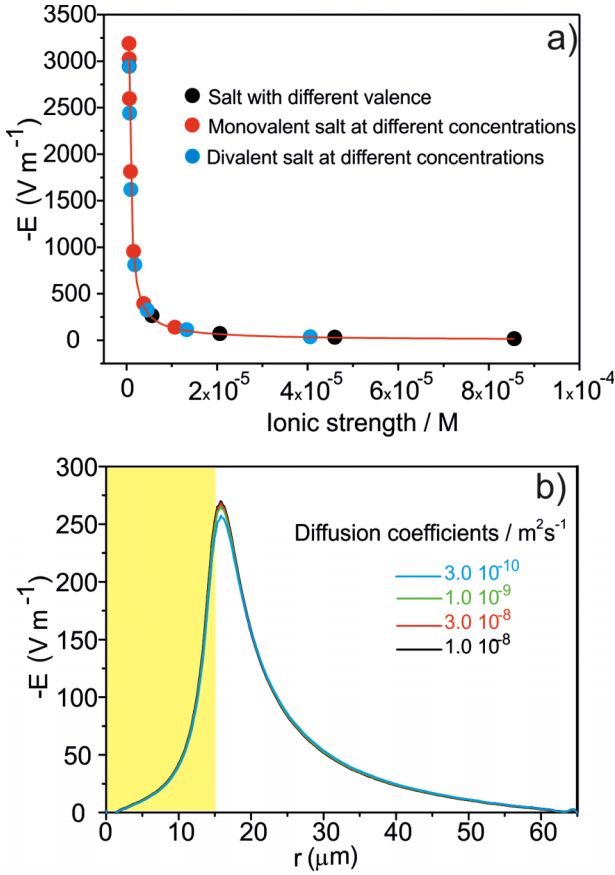
FIG. 6. (a) Maximum value of the radial electric field at 2 μm above the surface as a function of the ionic strength for different sets of data. The red line represents the data fitted according to Eq. (22). (b) Variation of the radial electric field with the diffusion coefficient of the salt D_A.

rather than on the total conductivity. According to the Nernst equation (Eq. (4)), the contribution of each species to the current density or flux is given by

$$j_i^e = eN_A z_i(-D_i \nabla C_i - z_i F \mu_i \nabla \varphi C_i + \mathbf{v} C_i), \quad (18)$$

where the terms on the right hand side represent the contributions of diffusion, migration and convection, respectively. The simulations show that, for the protons, the diffusion term is the dominant contribution to the current, and for all species, the contribution of convection is typically much smaller than the other two (see Fig. S4[44]). If we neglect the convection term, divide each flux by its diffusion coefficient, and add up the contribution of all species, we have

$$\sum_i \frac{j_i^e}{D_i} = -eN_A \nabla \left(\sum_i z_i C_i \right) - \frac{2N_A e^2}{k_B T} \left(\frac{1}{2} \sum_i z_i^2 C_i \right) \nabla \varphi. \quad (19)$$

The first term on the right hand side cancels out because of electroneutrality. Moreover, the dominant species contributing to the total current density are the protons since they are the reacting species (in fact we verified in the simulations that the net contribution to the current of the remaining ionic species is negligible). Hence

$$\sum_i \frac{j_i^e}{D_i} \approx \frac{j_{H^+}^e}{D_{H^+}} = -\frac{2N_A e^2}{k_B T} I \nabla \varphi \quad (20)$$

that finally leads to

$$E \approx \frac{j_{H^+}^e}{D_{H^+} \frac{2N_A e^2}{k_B T} I}, \quad (21)$$

where $E = -\nabla \varphi$ is the electric field and $I = \frac{1}{2} \sum_i z_i^2 C_i$ is the total ionic strength. We have fitted the results in Fig. 6(a) to a general equation,

$$E_r = 1/(a + bI). \quad (22)$$

The parameters obtained from the fit, namely, $a = -1.0 \times 10^{-4} \pm 6 \times 10^{-6}$ m/V, $b = 750 \pm 10$ m/VM, are approximately equal to the theoretical expectations ($a^{th} \approx 0$ m/V, $b^{th} = D_{H^+} \frac{2N_A e^2}{j_{H^+}^e k_B T} = 634$ m/VM), thus confirming the validity of this simple argument.

C. Effect of the rate constants of the anode and cathode

The variation of the rate constants can be thought as changes in the metals and their surface properties constituting the micropump. Figure 7(a) shows the maximum value of the radial electric field (just at the border of the Pt disk) when the rate constant of the anode is varied by three orders of magnitude. The supplementary material[44] also provides the radial electric field variation and the radial distribution of
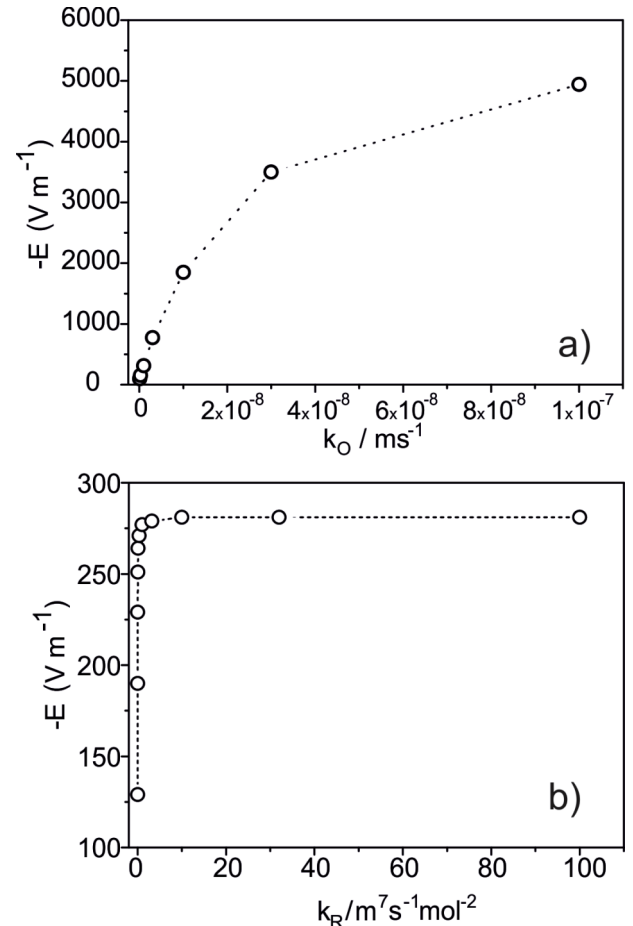

FIG. 7. Variation of the maximum radial electric field with (a) the anode rate constant k_O and (b) the cathode rate constant k_R.

the local proton concentration (Figures S5(a) and S5(b)[44]). As expected, since the anodic reaction rate k_O determines the proton production (see Fig. 1(a)), its increase leads to higher values of the proton concentration, of the electric field and consequently, of the pumping velocity. This progressive increase seems to reach a saturation/plateau at high values of k_O, when the overall reaction becomes limited by the cathode, that is no longer able to consume all the protons generated at the anode.

In contrast to the dramatic effects produced by the change in the anodic rate constant on the electrokinetic parameters, the variation of the cathode rate constant k_R affects in a lesser extent, as shown in Fig. 7(b) and Figs. S5(c) and S5(d) of the supplementary material.[44] An increase of 3 orders of magnitude in k_R, with respect to the reference value listed in Table I, does not lead to any significant change since the overall reaction seems to be limited by the anodic rate constant. Contrarily, a reduction of the cathodic rate constant k_R below the reference value decreases the pH (see supplementary material[44]) and the electric field up to a factor of 2, since the overall reaction rate becomes increasingly limited by the low cathodic reduction rates.

D. Effect of the hydrogen peroxide and the bulk proton concentration

Hydrogen peroxide is the fuel driving this catalytic pump. Its concentration controls the rate of the electrochemical reaction at the anode and cathode (Eqs. (9) and (10)), therefore greatly affecting the electric field (Fig. 8(a)), fluid velocity, and proton concentration (see supplementary material, Figures S6(a) and S6(b)[44]). Similar to the effect of the rate constants, the increase of the electric field and fluid velocity with the fuel concentration is not linear in the whole range, reaching a saturation at higher hydrogen peroxide concentrations. Such tendency to saturation is more pronounced at a low salt concentration. That is in agreement with the theoretical findings of Sabass and Seifert[38] and the experimental data. An interpretation of this saturation has been given in the framework of a Michaelis-Menten like surface kinetics.[38]

The initial concentration of protons (or pH) in the bulk also impacts the results in two opposite directions. On the one hand, it can change the ionic strength which would reduce the electric field. But on the other hand, it increases the reduction rate at the cathode, thus enhancing the overall reaction. Judging from the results plotted in Fig. 8(b) (showing an increase of the electric field with the bulk proton concentration), the dominant effect is the increase of the reaction rate, leading to higher values of the electric field and accordingly those of the pumping velocity.

E. Effect of the size of the cathode and anode

As presented in Fig. 1, the typical layout of the micropump consists of a smaller metal disk with the role of cathode which is patterned on a bigger radius disk acting as the anode. For design purposes, it becomes very interesting to analyze the impact of the electrode sizes on the catalytic pumping.
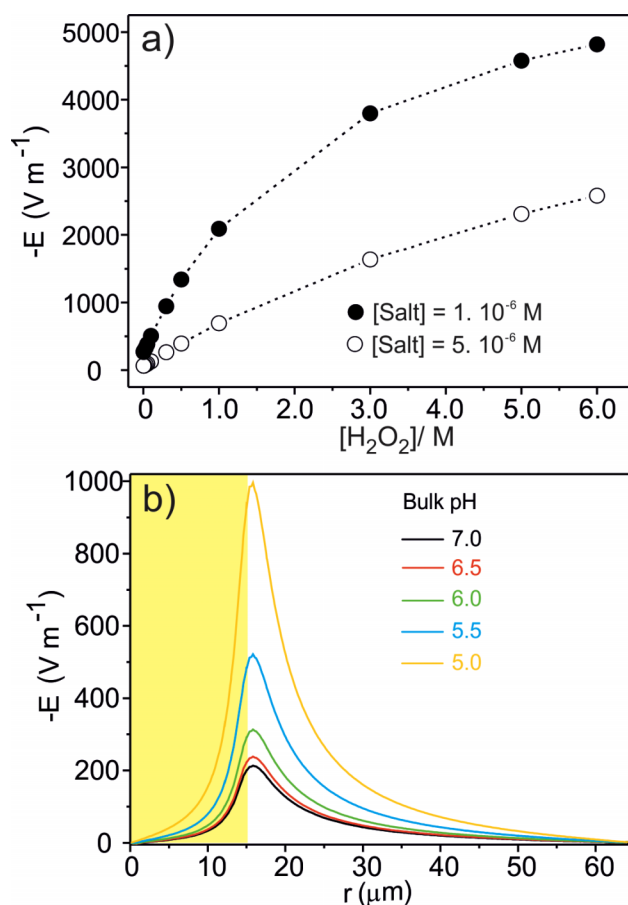

FIG. 8. (a) Dependence of the maximum radial electric field with the concentration of H_2O_2 at two different salt concentrations. (b) Dependence of the radial electric field with the bulk pH.

Figure 9(a) shows the variation of the electric field when the cathode radius is changed from 10 to 50 μm while keeping the anode radius at a constant value of 50 μm. We can observe that the radius of the disk has essentially a negligible influence on the electric field and fluid velocity at these conditions. This indicates that the overall reaction is certainly not limited by the cathode surface, in agreement with the results obtained for variations in the cathodic reaction rate represented in Fig. 7(b). However at very low cathodic rate constants (e.g., $k_R = 0.001$ m^{7}s^{-1}mol^{-2}), bigger changes in the electric field and fluid flow can be observed at small disk radius as shown in Fig. S7(b) (see supplementary material[44]). In this case, the overall reaction rate would be limited by the electron transfer at cathode and the disk radius (or area) acquires a crucial role for the cathode reaction.

The radius of the anode affects the electrokinetic parameters up to a certain value. Figure 9(b) show the effect of varying the anode radius on the electric field. In these simulations, the radius of the cathode disk was maintained at 15 μm and the anode radius was changed from 10 μm to 100 μm. Remarkable changes in the electric field can only be observed if the anode radius is well below 50 μm. However, the electric field and proton concentration (see supplementary material[44]) remain almost unchanged if we increase the anode radius beyond 50 μm. Consistent with our findings that diffusion is the dominant contribution to the
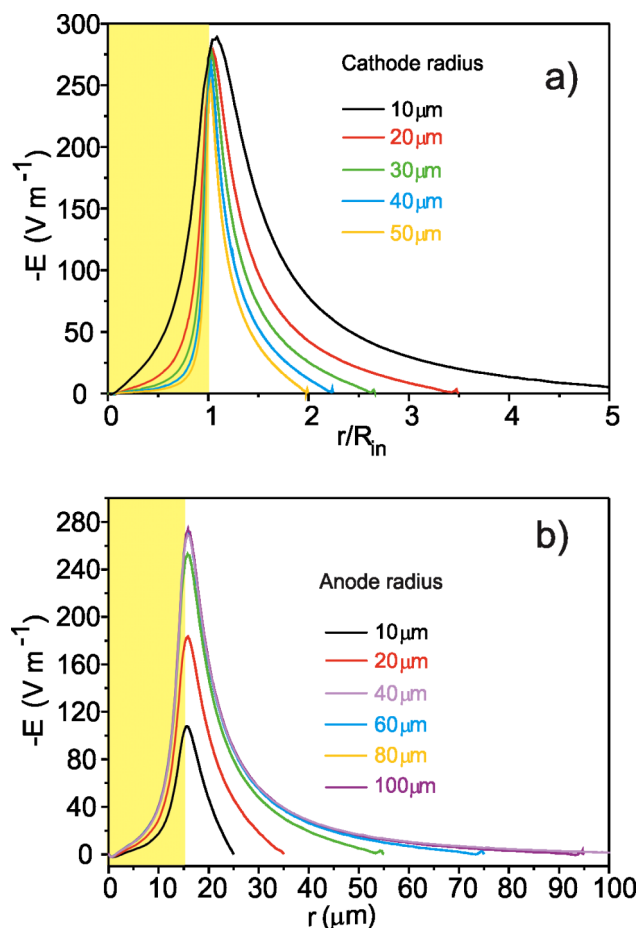
FIG. 9. Dependence of the radial component of the electric field with the radial distance for different values of: (a) the radius of the cathode R_{in}, for a fixed value of the radius of the anode of 50 μm and (b) the radius of the anode $R_{out} - R_{in}$, for $R_{in} = 15$ μm.

proton current and thus to the electric field, it seems that the important point is that the reaction establishes a gradient of protons and this gradient does not seem to change if we increase the area of the cathode or anode in excess of the minimum requirements needed to compensate the overall reactions (to balance the production and consumption of protons on both electrodes).

Accordingly, in an optimal design of a catalytic pump, it is very important to balance the reaction rates and the areas of both materials in such a way that none of them become rate limiting. But, beyond those requirements, there is no further advantage in increasing the size of the electrodes.

V. CONCLUSIONS

A systematic analysis of the influence of the different parameters involved in the chemomechanical actuation in catalytic pumps has been performed. We have shown that the fluid motion stems from a self-generated electro-osmosis induced by the chemical reactions, and it is thus very sensitive to the surface potential. The surface potential is not only the key parameter for setting the electric double layer and triggering the motion but also for setting the pumping strength and direction.

We have also shown that the electric field driving the electro-osmosis exists beyond the double layer and is originated by the diffusive proton flux from the anode to cathode rather than by the charge asymmetry between the anode and cathode inside the double layer. Surprisingly such an electric field and consequently the fluid flow are mainly controlled by the ionic strength and not by the conductivity of the fluid. That is supported by the clear dependence of such electrokinetic parameters on the concentration and valence of the salts but not on their diffusion coefficients.

There are other parameters which have a more obvious influence on the performance of the pump. In particular, the rate constants of the anode and cathode, the bulk concentration of protons, and the concentration of the peroxide fuel all have a positive influence on the electric field and the pumping velocity, both reaching a saturation. This saturation occurs when the limiting factor for the net proton flux is no longer the reaction rates at the electrodes, but rather the limits imposed by diffusion. In addition, for an optimal performance, a balance between the rates at the anode and cathode has to be fulfilled so that neither of them is limiting the reaction. That has a clear reflection on the relative surface of both electrodes, showing that beyond some size, there is no improvement or advantage in having larger electrodes. The electrode dimensions only exhibit remarkable effects at small sizes and very low redox constant rates.

All these theoretical findings can help to acquire a better understanding of the micropumps and provide useful hints or clues in the search, design, and optimization of novel catalytic devices.

[1]W. F. Paxton, S. Sundararajan, T. E. Mallouk, and A. Sen, Angew. Chem., Int. Ed. **45**, 5420 (2006).
[2]W. F. Paxton, A. Sen, and T. E. Mallouk, Chem. Eur. J. **11**, 6462 (2005).
[3]Y. Wang, R. M. Hernandez, D. J. Bartlett, J. M. Bingham, T. R. Kline, A. Sen, and T. E. Mallouk, Langmuir **22**, 10451 (2006).
[4]T. R. Kline, W. F. Paxton, Y. Wang, D. Velegol, T. E. Mallouk, A. Sen, and D. Velegol, J. Am. Chem. Soc. **127**, 17150 (2005).
[5]T. R. Kline, J. Iwata, P. E. Lammert, T. E. Mallouk, A. Sen, and D. Velegol, J. Phys. Chem. B **110**, 24513 (2006).
[6]W. F. Paxton, P. T. Baker, T. R. Kline, Y. Wang, T. E. Mallouk, and A. Sen, J. Am. Chem. Soc. **128**, 14881 (2006).
[7]S. Sánchez and M. Pumera, Chem. Asian J. **4**, 1402 (2009).
[8]J. Wang, ACS Nano **3**, 4 (2009).
[9]M. Pumera, Nanoscale **2**, 1643 (2010).
[10]J. Wang and K. M. Manesh, Small **6**, 338 (2010).
[11]S. J. Ebbens and J. R. Howse, Soft Matter **6**, 726 (2010).
[12]Y. Mei, A. A. Solovev, S. Sanchez, and O. G. Schmidt, Chem. Soc. Rev. **40**, 2109 (2011).
[13]S. Sengupta, M. E. Ibele, and A. Sen, Angew. Chem., Int. Ed. **51**, 8434 (2012).
[14]W. Wang, W. Duan, S. Ahmed, T. E. Mallouk, and A. Sen, Nano Today **8**, 531 (2013).
[15]T. Lee, M. Alarcon-Correa, C. Miksch, K. Hahn, J. G. Gibbs, and P. Fischer, Nano Lett. **14**, 2407 (2014).
[16]M. Guix, C. C. Mayorga-Martinez, and A. Merkoci, Chem. Rev. **114**, 6285 (2014).
[17]J. Wu, D. Balasubramanian, D. Kagan, K. M. Manesh, S. Campuzano, and J. Wang, Nat. Commun. **1**, 36 (2010).

[18]J. Simmchen, A. Baeza, D. Ruiz, M. J. Esplandiu, and M. Vallet-Regí, Small **8**, 2053 (2012).

[19]W. Gao and J. Wang, ACS Nano **8**, 3170 (2014).

[20]S. Sanchez, A. A. Solovev, S. Schulze, and O. G. Schmidt, Chem. Commun. **47**, 698 (2011).

[21]J. Wang, Lab Chip **12**, 1944 (2012).

[22]L. Soler, V. Magdanz, V. M. Fomin, S. Sanchez, and O. G. Schmidt, ACS Nano **7**, 9611 (2013).

[23]L. Soler and S. Sanchez, Nanoscale **6**, 7175 (2014).

[24]D. Kagan, S. Campuzano, S. Balasubramanian, F. Kuralay, G. U. Flechsig, and J. Wang, Nano Lett. **11**, 2083 (2011).

[25]S. Balasubramanian, D. Kagan, C. M. J. Hu, S. Campuzano, M. J. Lobo-Castañon, N. Lim, D. Y. Kang, M. Zimmerman, L. F. Zhang, and J. Wang, Angew. Chem., Int. Ed. **50**, 4161 (2011).

[26]S. Campuzano, J. Orozco, D. Kagan, M. Guix, W. Gao, S. Sattayasamitsathit, J. C. Claussen, A. Merkoci, and J. Wang, Nano Lett. **12**, 396 (2012).

[27]D. Kagan, R. Laocharoensuk, M. Zimmerman, C. Clawson, D. Balasubra-manian, D. Kong, D. Bishop, S. Sattayasamitsathit, L. F. Zhang, and J. Wang, Small **6**, 2741 (2010).

[28]W. Gao, D. Kagan, O. S. Pak, C. Clawson, S. Campuzano, E. Chuluun-Erdene, E. Shipton, E. E. Fullerton, L. F. Zhang, E. Lauga, and J. Wang, Small **8**, 460 (2012).

[29]W. Gao and J. Wang, Nanoscale **6**, 10486 (2014).

[30]E. L. K. Chng, G. J. Zhao, and M. Pumera, Nanoscale **6**, 2119 (2014).

[31]M. J. Xuan, J. X. Shao, X. K. Lin, L. R. Dai, and Q. He, ChemPhysChem **15**, 2255 (2014).

[32]A. Afshar-Farniya, M. J. Esplandiu, D. Reguera, and A. Bachtold, Phys. Rev. Lett. **111**, 168301 (2013).

[33]J. L. Moran, P. M. Wheat, and J. D. Posner, Phys. Rev. E **81**, 065302 (2010).

[34]J. L. Moran and J. D. Posner, J. Fluid Mech. **680**, 31 (2011).

[35]A. Brown and W. Poon, Soft Matter **10**, 4016 (2014).

[36]S. Ebbens, D. A. Gregory, G. Dunderdale, J. R. Howse, Y. Ibrahim, T. B. Liverpool, and R. Golestanian, Europhys. Lett. **106**, 58003 (2014).

[37]R. Golestanian, T. B. Liverpool, and A. Adjari, New J. Phys. **9**, 126 (2012).

[38]B. Sabass and U. Seifert, J. Chem. Phys. **136**, 214507 (2012).

[39]E. Yariv, Proc. R. Soc. A **467**, 1645 (2011).

[40]J. L. Moran and J. D. Posner, Phys. Fluids **26**, 042001 (2014).

[41]S. Thakur and R. Kapral, J. Chem. Phys. **135**, 024509 (2011).

[42]P. H. Colberg and R. Kapral, Europhys. Lett. **106**, 30004 (2014).

[43]A. Afshar Farniya, M. J. Esplandiu, and A. Bachtold, Langmuir **39**, 11841 (2014).

[44]See supplementary material at http://dx.doi.org/10.1063/1.4944319 for further details of the parameters affecting the electrokinetic process.